



## Mesh quality oriented 3D geometric vascular modeling based on parallel transport frame

Jixiang Guo<sup>a,\*</sup>, Shun Li<sup>b</sup>, Yim Pan Chui<sup>b</sup>, Jing Qin<sup>b,c</sup>, Pheng Ann Heng<sup>b</sup>

<sup>a</sup> College of Computer Science, Sichuan University, Chengdu 610065, Sichuan, China

<sup>b</sup> Department of Computer Science and Engineering, The Chinese University of Hong Kong, Shatin, Hong Kong

<sup>c</sup> Center for Human–Computer Interaction, Shenzhen Institutes of Advanced Technology, Chinese Academy of Sciences, Shenzhen, China



### ARTICLE INFO

#### Article history:

Received 9 March 2011

Accepted 4 April 2013

#### Keywords:

Geometric vascular modeling

Mesh quality

Parallel transport frame

Bifurcation and trifurcation

Non-concave and self-intersection free mesh

### ABSTRACT

While a number of methods have been proposed to reconstruct geometrically and topologically accurate 3D vascular models from medical images, little attention has been paid to constantly maintain high mesh quality of these models during the reconstruction procedure, which is essential for many subsequent applications such as simulation-based surgical training and planning. We propose a set of methods to bridge this gap based on parallel transport frame. An improved bifurcation modeling method and two novel trifurcation modeling methods are developed based on 3D Bézier curve segments in order to ensure the continuous surface transition at furcations. In addition, a frame blending scheme is implemented to solve the twisting problem caused by frame mismatch of two successive furcations. A curvature based adaptive sampling scheme combined with a mesh quality guided frame tilting algorithm is developed to construct an evenly distributed, non-concave and self-intersection free surface mesh for vessels with distinct radius and high curvature. Extensive experiments demonstrate that our methodology can generate vascular models with better mesh quality than previous methods in terms of surface mesh quality criteria.

© 2013 Elsevier Ltd. All rights reserved.

### 1. Introduction

Three-dimensional geometric vascular models have many important applications such as disease diagnosis, medical device design and simulation-based vascular interventional radiology (VIR) training and planning. A number of methods have been proposed to generate vascular models from medical images. In early studies, marching cubes (MC) [1] and its variations [2,3] were applied to extract iso-surface of vascular tree from volume images. Although the results are useful for pathological diagnosis, the narrow vessels are usually skipped, resulting in that they cannot provide integrated topology information of vascular tree, which is critical for the application of VIR simulation [4].

Another kind of method is to construct a geometric model using the skeleton of vascular tree and its radius information, from which an approximated surface model can be constructed either explicitly or implicitly [5]. The early popular explicit symbolic approaches are proposed in [6–8], where cylinders or truncated cones are employed to create vascular models. However, either cylinder or truncated cones may result in discontinuities at

furcations. Moreover, the smoothness of the generated surface is poor. To tackle these problems, methods based on parametric and implicit surface are proposed, including B-spline surface [9], subdivision surface [10,11], simplex meshes [12] and convolution surface [13–16]. Although these implicit methods can achieve a relatively smoother transition at furcations, the realism and accuracy of the built model cannot be guaranteed, as the furcation models in these methods are arbitrarily defined without any quantitative criteria [17].

Frame based modeling is another kind of explicit method. In [18,19], surface sweeping algorithm based on frenet frame is adopted to generate vascular network models. However, due to the un-definition of frenet frame at inflection points, the generated model suffers from vessel twisting problem. Later, parallel transport frame was employed [20] to generate a twisting-free vessel surface. It can overcome the non-definition and non-continuity problem of frenet frame. Although this method can reconstruct geometrically and topologically accurate 3D vascular models, problems of cross sectional self-intersection, concave surface mesh and frame mismatch still frequently occur at furcations and vessels with distinct radius and high curvature, which may greatly compromise the mesh quality of the resultant models.

Vascular furcation is essential to vascular surgery planning and treatment. A bifurcation model was constructed in [19] by using three Bézier curves as the bifurcate trajectory. The end points on

\* Corresponding author. Tel.: +86 18280331854.

E-mail addresses: guojixiang@gmail.com, guojixiang@scu.edu.cn (J. Guo), lis@cse.cuhk.edu.hk (S. Li), ypcchui@cse.cuhk.edu.hk (Y.P. Chui), jing.qin@siat.ac.cn (J. Qin), pheng@cse.cuhk.edu.hk (P.A. Heng).

each Bézier curve are computed according to the bifurcate point and each branching diameter. Unfortunately, this method does not work well for all the bifurcation cases. For a bifurcation with thick branching or if the bifurcate angle of its two children branchings is too small, the base half tube will be warped and the cross sectional self-intersection problem is serious. The main cause for this problem is inaccurate construction of bifurcation skeletons.

In human vascular system, although most of the branchings are bifurcations, trifurcation also exists in coronary arteries, carotid artery and abdominal aorta. Especially, the vascular aneurysm generally arises at the carotid artery bifurcation and forms a trifurcation [21]. To our knowledge, very little research has been involved in vascular trifurcation modeling. One of them is developed in [22], where solid NURBS based trifurcation templates were built for whole blood vessel construction. However, this kind of model is not appropriate for simulation of VIR procedure due to its solid property. Moreover, the transition at furcations is not continuous and smooth, and the built mesh at transition region is usually concave because of the pre-construction of hexahedral control meshes in vascular modeling procedure.

Some methods were proposed for solving cross sectional self-intersection. A simple stitching method was proposed in [23,24], but sharp edges might appear after stitching and this made the final surface mesh harsh and cracked. In recent work [25], a new method was proposed to deal with self-intersection by weakening the orthogonality constraint between cross-section plane and trajectory curve. But this method may repeat itself in an endless cycle, and in some cases even user-specified maximal iteration number is reached, the self-intersection still exists. Moreover, the swept mesh after the frame adjusting is not smooth as a concave inner surface may be produced.

In summary, the above-mentioned methods can more or less reconstruct geometrically and topologically accurate 3D vascular models, but the mesh quality still cannot sufficiently fulfill the

requirement of numerical simulation [26,27]. To bridge this technical gap, we propose a set of methods to deal with this problem based on parallel transport frame. After vascular skeleton extraction and framing based on the segmented vascular volume data, an improved bifurcation modeling method is proposed to solve warping and self-intersection problem of the half tube. More important, two novel trifurcation modeling methods are proposed to handle the cases that the four branching end points are coplanar or not coplanar, respectively. A frame blending scheme is further implemented to solve the mesh twisting and holes caused by frame mismatch of two successive junctions. On the other hand, an adaptive sampling algorithm combined with a mesh smoothness criteria guided frame tilting scheme is proposed to construct non-concave, self-intersection free and evenly distributed surface mesh for vessels with distinct radius and high curvature. Extensive experiments demonstrate that our methodology can generate vascular models with better mesh quality than previous methods in terms of mesh planarity criterion, mesh smoothness criterion and shape quality. The rest of the paper is organized as follows. Section 2 describes the details of our mesh quality oriented vascular modeling procedure. Section 3 provides results and discussion. Section 4 draws conclusion.

## 2. Mesh quality oriented vascular modeling

Our mesh quality oriented vascular modeling procedure includes three steps: vascular skeleton extraction and framing, furcation modeling and non-concave and self-intersection free surface construction.

### 2.1. Vascular skeleton extraction and framing

The vascular skeleton and radius information are extracted from vascular volume data, which are manually segmented from computed tomographic angiography (CTA) volumes by medical trainees. Then, we develop an automatic centerline calculation algorithm based on a well-known 3D topological thinning algorithm [28] to locate skeleton voxels within the 3D vascular volume. The skeleton voxels are smoothed by a sliding average filter [17] in order to avoid jaggedness in voxel presentation. The smoothly adjacent skeleton points are connected to form a vascular tree.

Considering the efficiency of our modeling method, only a subset of the skeleton points are employed (we call them feature points hereafter). We select these feature points based on the local curvature along skeleton curve. The process is illustrated in Fig. 1. For initial  $n$  skeleton points  $p_0, p_1, \dots, p_{n-1}$  (black and green points), with approximated local curvature defined as  $\|p''_i\|$ , a feature point is selected when condition  $\|p''_i\| > \xi$  is satisfied, where  $\xi$  denotes the curvature threshold. Then, a number of Bézier segments are fitted onto the selected feature points (black points). Feature points are exploited as the end points of Bézier segment. Extra

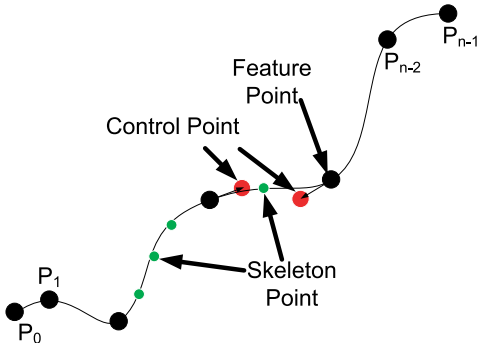


**Fig. 1.** Feature point selection. Black and green points denote the skeleton points; black points denote the feature points, and red points denote the control points for Bézier segment. (For interpretation of the references to color in this figure caption, the reader is referred to the web version of this article.)

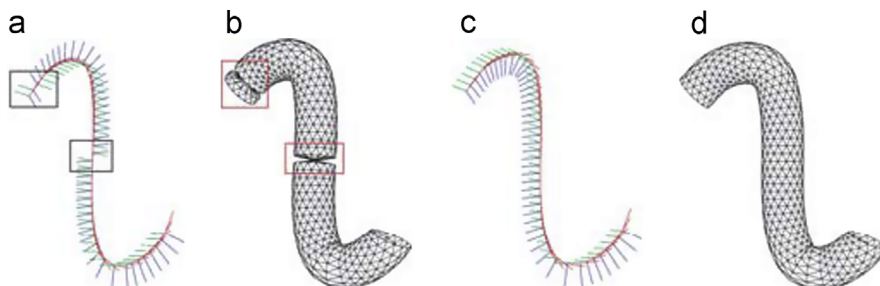


**Fig. 2.** Frames on a curve: (a) frenet frames, (b) swept surface mesh based on frenet frame, (c) parallel transport frames and (d) swept surface mesh based on parallel transport frame.

control points (red points) are computed through colinearizing the tangents of local end points between adjacent segments so that a  $C^1$  continuous curve is generated.

Creating optimal frame on a curve has been widely used to create ribbons and tubes in computer graphics domain. Such moving coordinate frame is defined by the curve geometry itself and composed of several orthogonal vectors along a curve. The well-known Frenet frame, i.e. TNB frame, which is composed of three unit vectors tangent ( $T$ ), normal ( $N$ ) and bi-normal ( $B$ ), suffers from the non-definition and non-continuity at zero-second derivative points (usually called inflection points) [29], which may greatly affect the mesh quality of final models. For example, as shown in Fig. 2(a) and (b), the frame before and after an inflection point is totally different and the corresponding surface mesh swept along the curve is twisted at the inflection point. There is no easy way to define a unique continuous Frenet frame over the whole curve. Due to the geometric complexity of vascular structure, Frenet frame is not suitable for vascular modeling.

Parallel transport frame was early proposed in [30], which properly solved the problems that occurred for Frenet frame on a curve with inflection points and can be well defined along the curve. It was originated from the notion of transporting a vector along a smooth curve as parallel to itself as possible [31]. The basic idea is, the tangent vector  $T(t)$  for a given curve is unique, therefore any orthogonal vectors  $(N(t), B(t))$  can be chosen in the plane perpendicular to  $T(t)$  at the beginning point. As long as the derivatives of  $(N(t), B(t))$  depend only on  $T(t)$  and not each other, they can vary smoothly throughout the path regardless of the curvature. Hence, when an initial frame is given, the subsequent frames will be generated sequentially, by computing new position  $P(t)$  and tangent  $T(t)$  on the curve. The old reference frame is then rotated such that the old tangent aligns itself with the new tangent. The rotation creates a new  $N(t)$  and  $B(t)$ , which, with the new  $P(t)$  and  $T(t)$ , define a new reference frame. Repeating the operation, a series of frames along a curve is created (Fig. 2(c)), which is then used to sweep the surface mesh according to the following Eq. (1) [32]:

$$\Gamma(t, \theta) = Z(t) + r(t)(\cos \theta N(t) + \sin \theta B(t)) \quad (1)$$

where  $t \in [0, 1]$ ,  $\theta \in [0, 2\pi]$ ;  $Z(t)$  represents a Bézier segment;  $r(t)$  denotes the radius of the blood vessel, which can be determined from the original patient data. Fig. 2(d) shows the resultant surface-swept curve based on the parallel transport frames. Compared with Fig. 2(b), the discontinuity problem is well solved.

## 2.2. Furcation modeling

Vascular furcation is a particular structure in complex vascular system, which is diversiform due to different angles of furcation and varying diameters of tubular vessels intersected at it. Therefore, building a furcation model which is with well mesh quality and can be glued with tubular branching seamlessly and smoothly is a challenging task.

### 2.2.1. Bifurcation

For bifurcation modeling, we employ the algorithm proposed in [19] with an improvement to avoid self-intersection in some specific cases. In this algorithm, bifurcation model is generated from a control skeleton which is composed of three Bézier curves as shown in Fig. 3(a), where  $O$  is the joint point of the central lines of the three branchings at the bifurcation;  $W_i$ ,  $i \in \{1, 2, 3\}$  are end points of the control skeleton; and  $U_i$ ,  $i \in \{1, 2, 3\}$  are control points. Fig. 3(d) shows the bifurcation model generated on the control skeleton.

In original algorithm,  $W_i$ ,  $i \in \{1, 2, 3\}$  are selected on the centerlines of three branchings according to a principle that the three distance values  $\|OW_1\|$ ,  $\|OW_2\|$ ,  $\|OW_3\|$  are in the same ranges of their corresponding branch diameters [19]. However, this method does not work well when the bifurcation angle is closer to an acute angle or the difference among the three diameters is distinct. For example, as shown in Fig. 3(b), as the angle of the bifurcation is too small, the frames along the control skeleton are constructed with obvious self-intersection, resulting in a twisted surface model (Fig. 3(e)).

To alleviate this problem, first, we compute the end points in consideration of the diameters of all branchings. After sorting the diameters of all branchings, we compute the end point on each branching according to the following rules: (1) the end point on

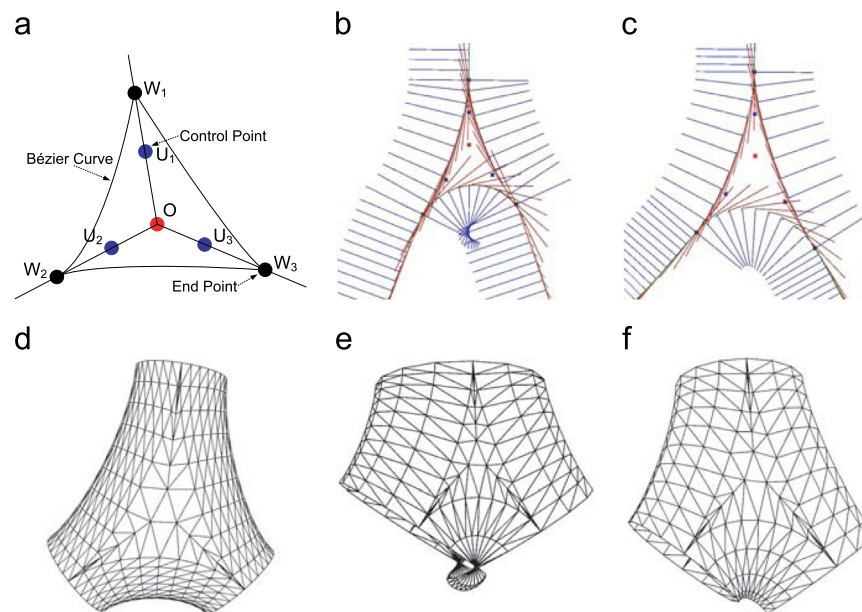


**Fig. 3.** Bifurcation modeling: (a, d) control skeleton of the bifurcation and generated bifurcation model based on it, (b, e) frames and control skeleton at bifurcation with self-intersection constructed by method [19] and corresponding bifurcation model built by our method, (c, f) frames and control skeleton at bifurcation free of self-intersection constructed by our method and corresponding bifurcation model built by our method.

centerline of the thickest tubular branching is computed by using the smallest diameter, (2) the end point on the centerline of narrowest tubular branching is computed by using the largest diameter and (3) for the third end point, if the diameter of its branching is close to the thickest one, the smallest diameter is used, otherwise the largest diameter is used. Second, a corrective process is further performed to resolve the cross sectional self-intersection problem. Each two end points are moved up or down along the branchings simultaneously until the corresponding cross sections at end points do not intersect with each other, to avoid the half-tube surface warping and cross sectional self-intersection.

Finally, a cubic triangular Bézier patch is constructed by the end points  $W_i$ , the joint point  $O$  and sharing the internal control points  $U_i$  with Eq. (2), which is applied to fill the triangular holes. The sharing of control points can achieve a smooth transition of the half tubes and the triangular surface, and the final bifurcation model is built by three half-swept tubes and the triangular Bézier patches. Fig. 3(c) and (f) shows the improved control skeleton and the bifurcation model generated from it. Compared with Fig. 3(b) and (e), the self-intersection problem is well resolved and the final model is smoother.

$$\begin{aligned} T(s, t, \mu) | (s \in [0, 1], t \in [0, 1], \mu \in [0, 1], s + t + \mu = 1) \\ = W_1 * t^3 + 3 * U_1 * s * t^2 + 3 * U_1 * t^2 * \mu \\ + 3 * U_2 * s^2 * t + 6 * O * s * t * \mu + 3 * U_3 * t * \mu^2 \\ + W_2 * s^3 + 3 * U_2 * s^2 * \mu + 3 * U_3 * s * \mu^2 + W_3 * \mu^3. \end{aligned} \quad (2)$$

## 2.2.2. Trifurcation

Two trifurcation models are built to handle two cases: (1) four end points on the tubular branchings are quasi-coplanar and (2) the four end points are not coplanar. A quadrilateral control skeleton is constructed for the first case and a tetrahedral control skeleton is constructed for the second case. The maximal angle of any two planes which are defined by three of four end points is used to check which model will be appropriate, a threshold of 10° is used in this paper. The end points in the two trifurcation control skeletons are computed by the same algorithm as used for bifurcation.

The quadrilateral control skeleton is composed of four 3D Bézier curves, as shown in Fig. 4(a), where,  $W_i$ ,  $i \in (1, 2 \dots 4)$  are the end points,  $U_i$ ,  $i \in (1, 2 \dots 4)$  are the control points,  $O$  is the joint point. To obtain a continuous mesh model, a Bézier patch is employed to fill the quadrilateral holes. The traditional Bézier patch illustrated in Fig. 4(b) is defined by  $4 \times 4$  control points  $P_{ij}$ ,  $i, j \in (0, 1 \dots 3)$ , which are connected to form four rows and four columns. Each row or column can be seen as a separate 3D Bézier curve. In our specific case, the Bézier patch is constructed as follow.  $W_i$  is used as the corner points of the Bézier patch (black points).  $V_i$ ,  $i \in (1, 2 \dots 4)$ , which are used as the internal control points for Bézier patch (red points), are computed as the middle point of  $U_i$  and the joint point  $O$ . The control points  $U_i$  are shared by the linked edge Bézier curves (bold curves in Fig. 4(b)). For example, the two control points  $P_{1,0}(W_1)$  and  $P_{0,1}(U_1)$  are represented by one point  $U_1$ , similarly for other edge control points (blue points) illustrated in Fig. 4(b). Therefore, the Bézier patch can be represented as Fig. 4(c). Fig. 4(d) shows the trifurcation model built by sweeping four half-tubes and triangulating the Bézier patch.

The tetrahedral control skeleton is composed of six Bézier curves, as shown in Fig. 5(a). Half swept tube is not appropriate here, as three Bézier skeletons are jointed at one end point  $W_i$ ,  $i \in (1, 2 \dots 4)$ . Fig. 5(b) and (c) shows how to sweep a proper tube region for each skeleton curve. First, the frames along each Bézier curve can be computed by parallel transport algorithm (Fig. 5(b)). As the tangent vector at the end point is fixed (which is confirmed by the  $C^1$  continuity of whole vascular skeleton), the

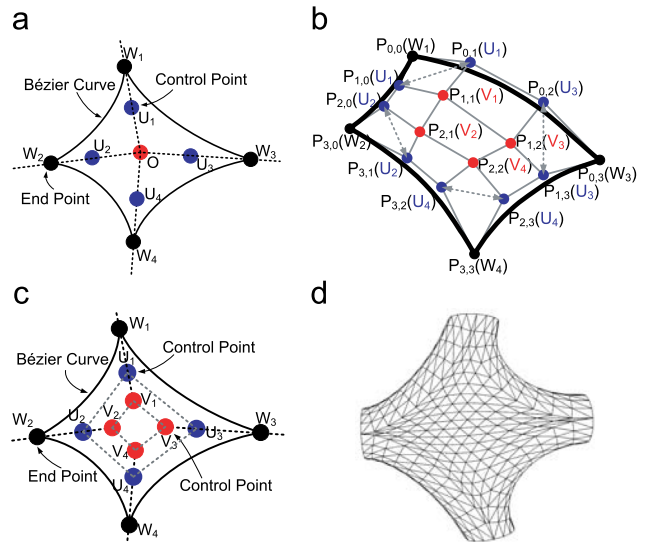


**Fig. 4.** Trifurcation modeling based on coplanar end points: (a) quadrilateral control skeleton, (b) Bézier patch used to fill the hole, (c) control skeleton for Bézier patch and (d) trifurcation model generated from the quadrilateral control skeleton. (For interpretation of the references to color in this figure caption, the reader is referred to the web version of this article.)

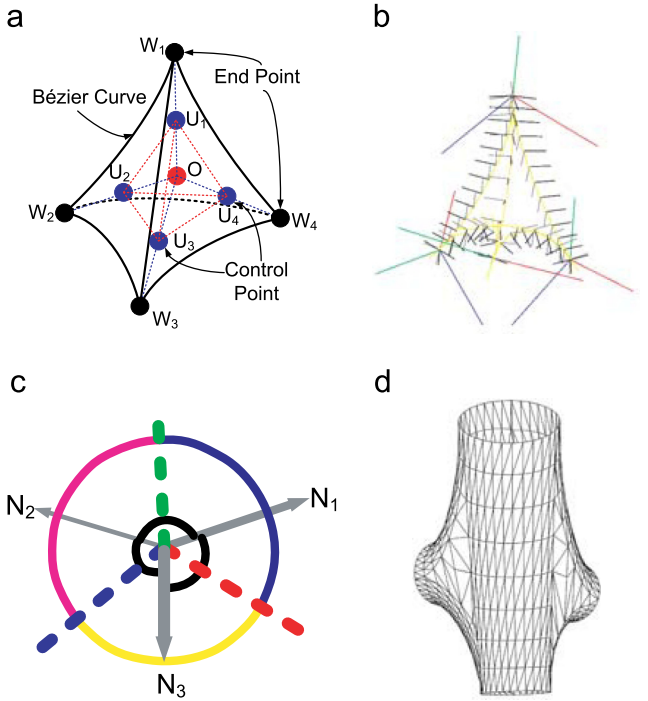


**Fig. 5.** Trifurcation modeling based on non-coplanar end points: (a) tetrahedral control skeleton, (b) frames along the tetrahedral skeleton, (c) cross section at a point on the control skeleton and (d) built trifurcation model.

normal and bi-normal vectors of the three Bézier curves intersected at end point  $W_i$  are on a same cross section, i.e. on a same plane on the basis of the orthogonality of the frame vectors. Fig. 5(c) illustrates the cross section at a common end point  $W_i$ , where  $N_j$ ,  $j \in (1, 2, 3)$  are the normal vectors of three Bézier curves jointed at  $W_i$ . Then three separating vectors can be obtained as the average vector of adjacent normal vectors, denoted as dotted lines in Fig. 5(c). They separate a circular cross section to three regions for each Bézier curve, and we sweep the surface for the three regions to build the tube mesh for the trifurcation model. Finally,

triangular Bézier surface is used to fill the holes according to the geometry of the tetrahedra to build an integrate model, as shown in Fig. 5(d).

### 2.2.3. Frame blending between successive furcations

After creating the bifurcation/trifurcation model, we need glue furcation models with tubular branchings seamlessly to obtain a entire model of vasculature. In this procedure, one problem that we need to be carefully dealt with is the construction of the tube between two successive furcations where simple parallel transport would lead to a mismatch of frames at the two furcations. This means that the frame rotated starting from one furcation cannot be smoothly matched with that at another one.

In principle, the bi-directional frame lists for the internal tubular structure between the two furcations can be computed by parallel transporting algorithm starting from either of the two furcations. However, this method cannot avoid the mismatch problem. For example, Fig. 6(a) shows the top-down frame list computed beginning from the top bifurcation. From the enlarged view, it is observed that a mismatch generated at the connection point of the bottom bifurcation, where an included angle  $\theta$  is produced. Likewise, the bottom-up frame list computed beginning from the bottom bifurcation is shown in Fig. 6(b), where a more obvious mismatch is generated. Accordingly, the built mesh models based on either top-down frame list or bottom-up frame list are not continuous and smooth, as shown in Fig. 6(d) and (e). The tubular mesh cannot be glued with the furcations seamlessly and holes obviously exist in the enlarged view at the upper right of Fig. 6(e).

In light of this, a corrective procedure has to be exploited in order to resolve such mismatch problems. A parallel transport blending method is adopted to adjust all the frames along the skeleton of the tube between furcations so as to re-match the frames at furcations. The main idea is blending the bi-directional frame lists generated from each end together to get a smooth

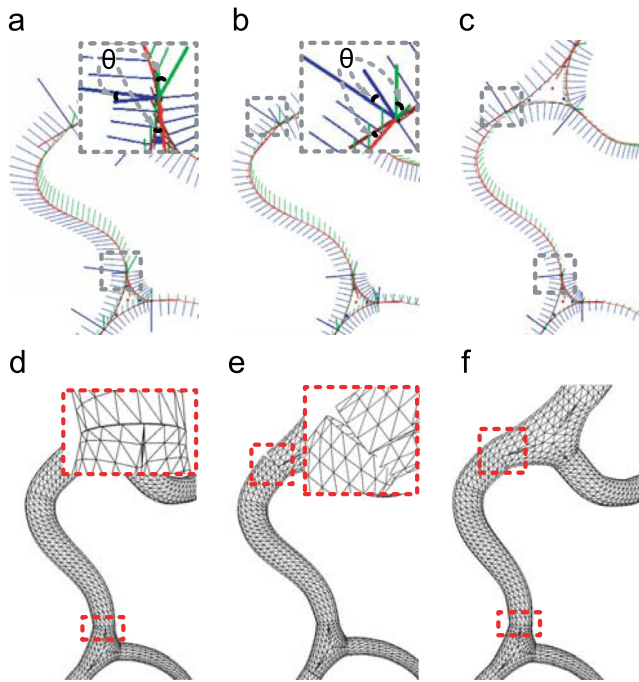


**Fig. 6.** Frame blending on the tube between successive furcations: (a) top-down frame list starting from the top bifurcation, (b) bottom-up frame list starting from the bottom bifurcation, (c) blended frame list, (d) mesh model built from the top-down frame list, (e) mesh model built from the bottom-up frame list and (f) mesh model built on the blended frame list.

frame list. Quaternion frame is employed for frame lists blending because the quaternionic representation provides an elegant formulation of geodesic slerp interpolation [29]. We first convert the TNB frame to a quaternion frame, which is a unit-length four-vector  $q = (q_0; q_1; q_2; q_3) = (q_0; \vec{q})$ . The quaternion frame exactly corresponds to one 3D coordinate frame. Then, we compute the quaternionic slerp interpolation on each corresponding frame along the two frame lists. We choose either the face normal vector or its reverse in the computation to ensure that the angle of the two end frames is an acute angle, which can make the rotational matching between the two furcations more smoother. Fig. 6(c) and (f) shows the frame list after frame blending and the corresponding mesh model. It can be clearly observed that the mismatch problem is well-solved and the quality of the mesh is greatly improved, especially at the furcation regions.

### 2.3. Self-intersection free surface mesh construction

Besides furcations, a vessel with distinct radius and high curvature may also greatly affect the mesh quality of final vascular model as cross sectional self-intersection problem always occurs at such a vessel. In order to obtain a mesh-size evenly distributed and continuous vessel surface, an adaptive sampling method is proposed based on local curve curvature and radius of every tubular branching of vascular tree. Then the frames are further adjusted according to mesh smoothness criteria in order to make sure that the final mesh is continuous, smooth and free of cross sectional self-intersection and no concave surface exists.

#### 2.3.1. Adaptive frame sampling

The process of our adaptive frame sampling method is as follows. For every tubular branching of the vascular tree, we first compute the curvature along its centerline curve according to Eq. (3) and the point with maximal curvature  $P_1$  can be found. Then we traverse the curve points from  $P_1$  forward and backward along the centerline to find the nearest point  $P_2$  which make sure that the cross section at this point does not intersect with the cross section at point  $P_1$ . We employ the voxel spacing of the CTA images as traversing step to make sure the found point  $P_2$  is the nearest one. The procedure is illustrated in Fig. 7(a), where  $T_i$  and  $N_i$  are the unit tangent and normal vectors at  $P_i$ ,  $i \in \{1, 2\}$ .

$$\kappa(t) = \frac{|r'(t) \times r''(t)|}{|r'(t)|^3} \quad (3)$$

To find  $P_2$ , an efficient algorithm is proposed to detect whether two cross sections intersect with each other. As shown in Fig. 7(c), for a point in a curve, the N-B plane, i.e. the cross section plane,

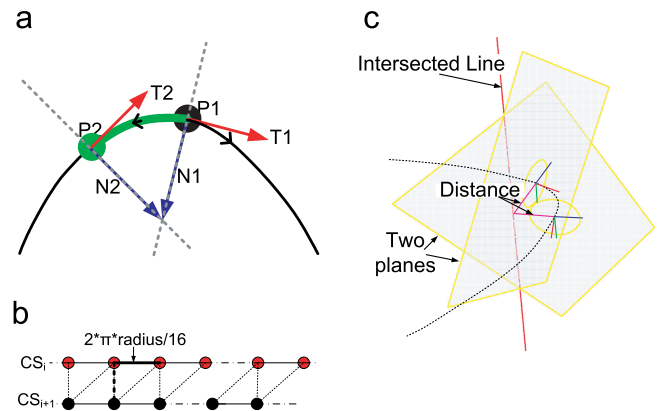


**Fig. 7.** (a) Finding two nearest adjacent points at the high curvature part that the cross sections at these point do not intersect, (b) connection of two adjacent cross sections and (c) adjacent cross sectional self-intersection detection.

can be defined by the position of the point with its tangent vector as the face normal. If two planes are parallel, then they will never intersect and  $P_2$  is found. Otherwise, there is an intersected line of these two planes. We compute the distance between  $P_1$  and the intersected line and the distance between the current traversing point and the intersected line, respectively, if both the distances are larger than the radius at these two points, self-intersection exists between these two cross sections. In this case, we traverse to next point until  $P_2$  is found.

Once  $P_2$  is found, it is conceivable to employ the arc length between  $P_1$  and  $P_2$  as the sampling step of this branching. However, although this can avoid self-intersection problem, it may cause another problem of deformed surface when the arc length is very large. In order to get a balance between the quality of the surface and the cross sectional self-intersection, radius information along the branching is considered into the selection of sampling step. The cross section (in short as CS, which is spread out as a line in Fig. 7(b), and  $i$  is the cross section index along the centerline curve) is equally divided into sixteen parts and 16 vertices are generated on each cross section. The triangular mesh is constructed by connecting corresponding vertices on neighboring cross sections. We select the minimal value between the arc length of  $P_1$  and  $P_2$  and the arc length of adjacent vertices on a cross section, which can be computed by  $2\pi * \text{Radius} / 16$ , as the sampling step for a vessel branching. As mentioned, although this method can alleviate the problem of deformed surface, it cannot totally avoid cross sectional self-intersection if the arc length of  $P_1$  and  $P_2$  is the larger one. In this case, we further adjust the frames based on a frame tilting scheme to solve it.

### 2.3.2. Frame tilting scheme

To maintain high mesh quality, our frame tilting scheme is proposed based on mesh smoothness criteria, which is measured by the dihedral angle between two adjacent faces. The detailed definition can be found in [26], that is, given a triangular surface, the value of smoothness  $S_e$  along a mesh edge  $e$  is defined in Eq. (4), where  $f$  means a triangular face and  $N$  is the unit face normal. The smoothness  $S_p$  at a vertex  $P$  is measured by minimum value of the smoothness of the mesh edge  $PP_i$  sharing  $P$  in Eq. (5). The mesh quality is better when the smoothness criteria is closer to 1, i.e. when the dot product of two unit face normals is closer to 1.

$$S_e = \frac{1 + \langle N_{f_1} \cdot N_{f_2} \rangle}{2} \quad (4)$$

$$S_p = \min_i S_{PP_i} \quad (5)$$

During modeling of complex vasculature, cross sectional self-intersection commonly occurs at high curvature parts of blood vessels or furcations with a sharp turning branching. For example, a visible self-intersection is presented in the highlighted region of Fig. 8(a) and (b) in frame view and mesh view respectively. Fig. 8(c) is the enlarged view of the highlighted region in Fig. 8(b). It can be observed that the built surface mesh is seriously deformed, some triangular patches are overlapped in green rectangular region. The difference of surface size in green and blue rectangular region is big, and long and narrow triangular surfaces are produced, which may greatly affect the accuracy of numerical simulation [33].

The frame tilting is implemented based on the parallel transport algorithm. First, the new tangent vector of a frame is computed according to Eq. (6), where  $\alpha$  is 0.5 at the index of highest curvature; for the frames before it,  $\alpha$  is set as the interpolation value between 0 and 0.5 according to index distance of current index away from the index of highest curvature and  $\beta = 1 - \alpha$ ; for the frames after it,  $\beta$  is set as the interpolation value and  $\alpha = 1 - \beta$ . Second, the new normal and bi-normal vectors are

generated according to parallel transport algorithm. The rotating axis  $\vec{B}$  is computed as the cross product of the old and new tangent by Eq. (8), and corresponding rotating angle  $\theta$  is computed by Eq. (7). Then, the new normal and bi-normal vectors are computed by rotating the old ones about  $\vec{B}$  by angle  $\theta$  in Eq. (9), which, with the new tangent, form a new frame. All frames along the skeleton except two end frames can be recomputed by these two steps. When all frames are updated, the smoothness value at the point of highest curvature is recomputed. This procedure will be repeated until the smoothness value at the highest curvature point reaches to a threshold defined by users. The above interpolation method used to compute the new tangent of a frame can prevent this iterative procedure from an endless cycle. Fig. 8(d-f) shows the results of our frame tilting scheme. It is observed that the cross sectional self-intersection has been well solved and the generated mesh surface is smoother and with more evenly distributed surface mesh size.

$$T_i^{new} = T_{i-1} * \alpha + T_{i+1} * \beta, (\alpha + \beta = 1) \quad (6)$$

$$\theta = \arccos(\langle T_i^{new} \cdot T_i^{old} \rangle) \quad (7)$$

$$\vec{B} = T_i^{new} \times T_i^{old} \quad (8)$$

$$N_i^{new} = R_{\vec{B}}^{\theta} N_i^{old} \\ B_i^{new} = R_{\vec{B}}^{\theta} B_i^{old} \quad (9)$$

## 3. Results and discussion

We conducted a series of experiments to demonstrate the feasibility of our proposed methodology qualitatively and quantitatively. We compared our method with a state-of-the-art method [25] for solving self-intersection problem in frame-based modeling and results demonstrate that ours is better in mesh quality. We also compared the mesh quality of our results of furcation modeling with a  $G^1$  bifurcation model [19], showed some cases of our trifurcation models, and discussed the efficiency of our methodology.

### 3.1. Mesh quality criteria

We focus on triangular surface mesh in this paper. It has been demonstrated that the mesh quality has a significant effect on the accuracy of numerical simulation especially for that based on finite element method [26,27]. To quantitatively compare our method with previous methods, we applied four common surface mesh quality criteria to do the comparison: (1) mesh planarity, (2) mesh deviation, (3) mesh smoothness and (4) shape quality. We briefly introduce their definition as follows and details can be found in [26].

- (1) Mesh planarity  $P_p$  at vertex  $P$  is used to compute the largest angle between the vertex normal  $N_p$  and its neighbor vertices' normal  $N_{p_i}$ . It is a criterion to evaluate the continuity of a mesh and can be computed by

$$P_p = \frac{1 + \min_i \langle N_p, N_{p_i} \rangle}{2} \quad (10)$$

- (2) Mesh deviation  $D_p$  at vertex  $P$  is used to compute the minimum value of the absolute value of the dot product of the vertex normal  $N_p$  and edge vectors  $V_{pp_i}$  along the direction  $\vec{PP_i}$ . It is also a criterion to evaluate the continuity of a mesh

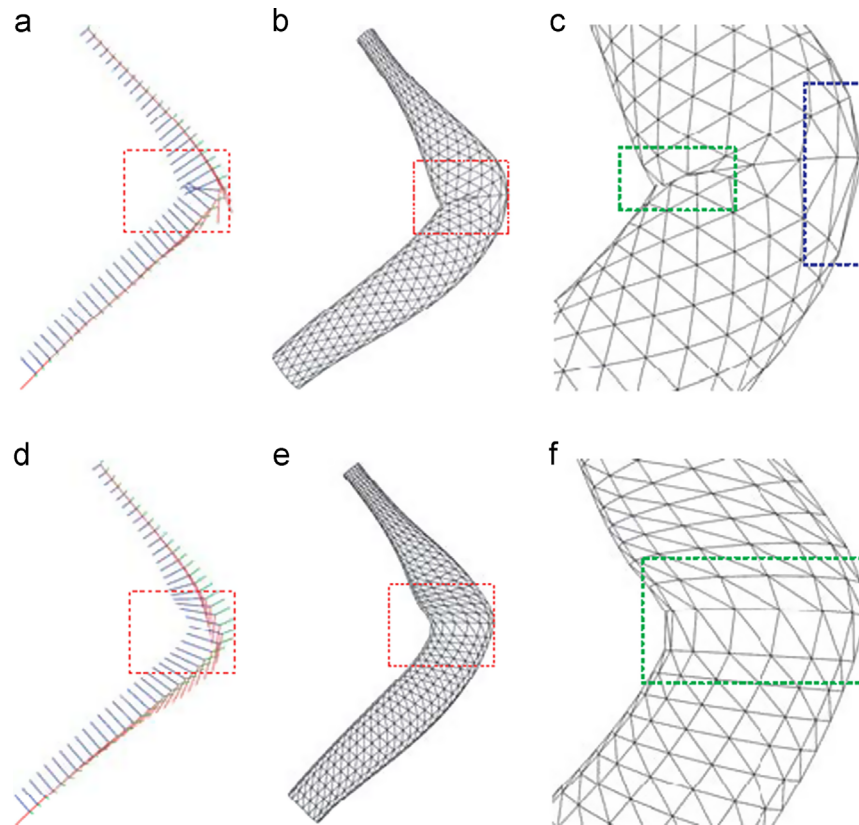


**Fig. 8.** (a) Frame list with self-intersection generated by parallel transport algorithm, (b) corresponding mesh built by the self intersected frame list, (c) enlarged view of left highlighted region, (d) frame list free of self-intersection after frame tilting, (e) resultant mesh after frame tilting and (f) enlarged view of left highlighted region. (For interpretation of the references to color in this figure caption, the reader is referred to the web version of this article.)

and can be computed by

$$D_p = 1 - \min_i |\langle N_p, V_{pp_i} \rangle| \quad (11)$$

- (3) Mesh smoothness is a criterion to evaluate the smoothness of a mesh and can be computed by Eq. (4).
- (4) Shape quality  $Q_{TF}$  is used to measure the similarity of a triangle to an equilateral triangle and can be computed by

$$Q_{TF} = \frac{6 \cdot A_{TF}}{P_{TF} \cdot h_{TF}} \quad (12)$$

where  $A_{TF}$  is the area of a triangle,  $P_{TF}$  is the half-perimeter of a triangle and  $h_{TF}$  is the longest edge length.

### 3.2. Comparative results on solving self-intersection

A qualitative comparison of the proposed method for solving cross sectional self-intersection with a state-of-the-art method presented in [25] is shown in Fig. 9. We employed cerebral vascular tree to do the comparison as it is one of the most complex vascular structure of human beings. Fig. 9(a) is the geometric cerebral vascular model generated based on our method. The self-intersection problems at the tubular segment of high curvature and the bifurcation with a sharp turning branching are analyzed.

Fig. 9(b-d) gives the comparison of the tubular segment with high curvature at the top highlighted region of cerebral vascular model. The frame list and the corresponding mesh model generated directly from parallel transport algorithm are shown in Fig. 9(b), in which a serious cross sectional self-intersection is observed. Fig. 9(c) shows the results generated by method [25]. Although self-intersection is somehow solved, a concave surface mesh is generated. Our resultant

frame list and corresponding mesh model are shown in Fig. 9(d). It is clear that not only the cross sectional self-intersection is solved, but also the generated surface model is smoother than the results of the method [25].

A more complex region is illustrated in Fig. 9(e-j). Besides a sharp turning branching, the self-intersection occurs at the joint of bifurcation and the tubular branching, as shown in the highlighted region of Fig. 9(e) and (h). The results generated by the method [25] are shown in Fig. 9(f) and (i). The cross sectional self-intersection is resolved, but it is observed in Fig. 9(f) that some cross sections are folded, especially in the left rectangular region, and the concave surface mesh still exists (Fig. 9(i)). Fig. 9(g) and (j) shows our results. It is shown that the self-intersection has been solved and the geometric continuity of the built surface mesh is improved greatly compared with the results of [25].

Table 1 shows the quantitative comparison of mesh evaluation results of the cerebral geometric mesh model built by [25] and our method. Although the advantage of our method is not obvious in the average values due to the large amount of mesh vertices, the minimal values of mesh quality criteria demonstrate that our method can greatly improve the mesh quality at special regions such as furcations and vessels with high curvature. It can be found in the table that the smoothness criterion has been remarkably improved by our method compared with the method [25], from 0.2053 to 0.9084. Accordingly the shape quality also has been greatly advanced from 0.024 to 0.247.

### 3.3. Evaluation of bifurcation modeling

Table 2 shows the quantitatively comparison of the bifurcation model constructed by method [19] and our method. Not only the minimal values of the mesh smoothness and shape quality have

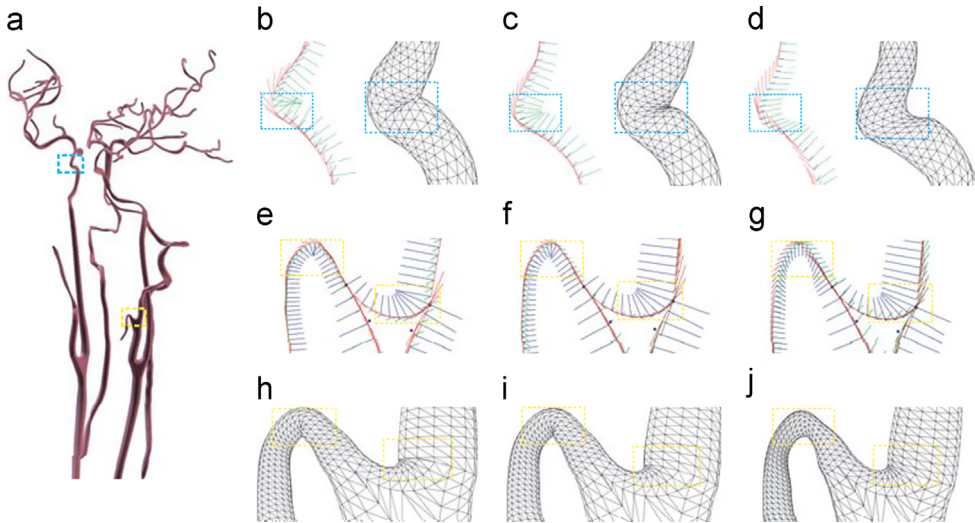


**Fig. 9.** Analysis of our proposed frame tilting method for solving the cross sectional self-intersection problems at the tubular segment of high curvature (highlighted region in light blue) and the bifurcation with a sharp turning branching (highlighted region in yellow): (a) geometric model of cerebral artery, (b) frames and mesh model with self-intersection generated by parallel transport algorithm, (c) frame and mesh model generated by method [25], (d) frames and mesh model generated by our method, (e) frames with self-intersection generated by parallel transport algorithm, (f) frames free of self-intersection generated by method [25], (g) frames free of self-intersection generated by our method, (h) built mesh model with self-intersection, (i) mesh model built by method [25] and (j) mesh model built by our method. (For interpretation of the references to color in this figure caption, the reader is referred to the web version of this article.)

**Table 1**

Comparison of mesh evaluation results of cerebral geometric models.

Criteria	$P_P$	$D_P$	$S_P$	$Q_{TF}$
	Min (avg)	Min (avg)	Min (avg)	Min (avg)
Method [25]	0.909 (0.9156)	0.8048 (0.94)	0.2053 (0.97)	0.024 (0.72)
Our proposed method	0.911 (0.9158)	0.8049 (0.94)	0.9084 (0.98)	0.247 (0.724)

**Table 2**

Comparison of mesh evaluation values of bifurcation modeling.

Criteria	$P_P$	$D_P$	$S_P$	$Q_{TF}$
	Min (avg)	Min (avg)	Min (avg)	Min (avg)
Method [19]	0.950313 (0.959056)	0.806704 (0.963069)	7.75591e-006 (0.788024)	0.00531402 (0.313234)
Our proposed method	0.953668 (0.959806)	0.832788 (0.967518)	0.958177 (0.966337)	0.0701835 (0.558561)

been improved significantly, but also the average mesh quality is advanced accordingly.

Moreover, we give some examples to demonstrate that our proposed trifurcation modeling methods can generate practical models with high mesh quality for medical application. Aneurysm is a common disorder in the wall of an artery and most aneurysms occur at the bifurcations and branches of the large arteries, a report of cerebral aneurysm location is given by [34]. The cerebral aneurysm generally appears as a “ballooning out” of a weakened blood vessel. In this situation, a bifurcation with the aneurysm forms a trifurcation. Fig. 10 shows two quadrilateral trifurcation models, where cerebral aneurysms commonly occur surrounding the circle of Willis. Fig. 10(a) shows the trifurcation model when aneurysm occurs at the carotid terminus, and Fig. 10(b) shows the model when aneurysm occurs at the basilar artery.

A vascular skeleton with a tetrahedral trifurcation model of hepatic artery is shown in Fig. 11, the extracted centerline and corresponding mesh model are shown in Fig. 11(a) and (b). The enlarged view of trifurcation skeleton and corresponding trifurcation model are shown in Fig. 11(c) and (d), it is clear that the tetrahedral trifurcation is well connected with four tubular branchings.

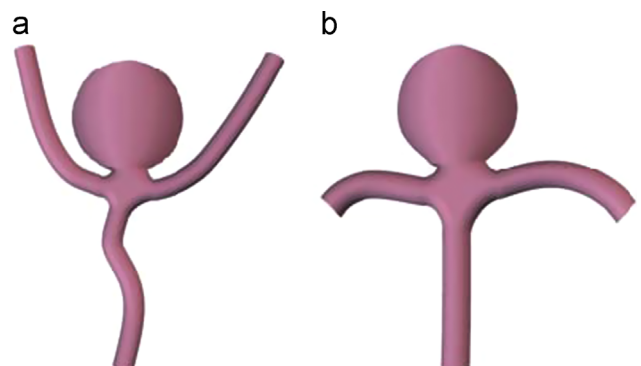


**Fig. 10.** Quadrilateral trifurcation examples for handling cerebral aneurysms: (a) aneurysm at carotid terminus and (b) aneurysm at basilar artery.

Finally, we record the time for building a vascular model with different number of vertices and triangle faces on a Intel(R) core (TM)2 CPU 2.66 GHZ system with 3.25 GB RAM. The experimental results, which are shown in Table 3, demonstrate that the modeling time is almost linearly related to the number of vertices/

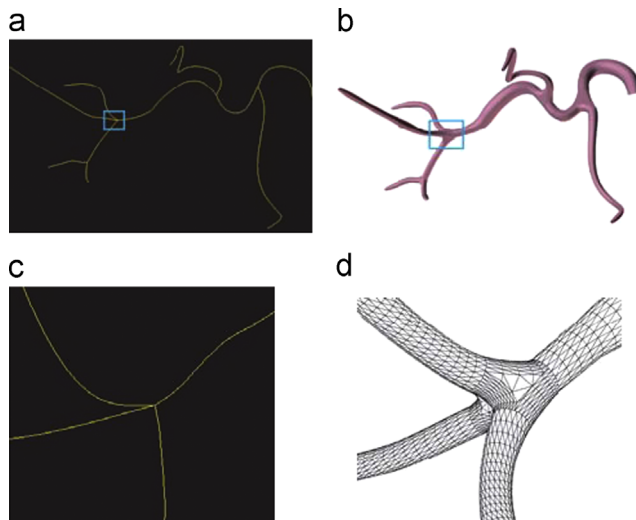


**Fig. 11.** (a) Extracted centerline skeleton from hepatic artery, (b) corresponding mesh model, (c) enlarged view of the highlighted tetrahedral trifurcation skeleton and (d) enlarged view of the highlighted mesh model with a tetrahedral trifurcation.

**Table 3**  
Efficiency measurement.

No. of skeleton points	No. of vertex	No. of triangles	Time(ms)
480	6518	12150	711.24
653	8885	16884	1094.87
953	18606	35499	3353.552
3425	59183	115098	9165.968

triangles within a surface mesh. The efficiency of our methodology can be guaranteed.

#### 4. Conclusions

Three-dimensional Bézier curve based bifurcation and trifurcation models are constructed in consideration of the vascular skeleton, vessel diameters and the angles of furcation, in this way the biological branching property of vascular geometry can be well guaranteed. To obtain a smooth rotational transition between two the successive furcations, a parallel transport blending algorithm is developed. The curve's curvature based adaptive sampling algorithm and mesh smoothness criteria guided frame tilting algorithm are proposed to avoid the problems of self-intersection and concave surface. Experiments on cerebral and hepatic vasculature demonstrate that our methodology can generate vascular models with better mesh quality than previous methods in terms of mesh quality criteria.

Some limitations exist in this study. Although our frame blending method has achieved a minimal rotational transition between two furcations, it cannot ensure the generated frame list totally free of twisting and in some cases we still need to manually adjust some frames after blending. In addition, to maintain the high mesh quality of the constructed models, a set of methods was proposed. The methodology might seem a bit complicated, but really it is just a number of simple steps. The implementation of whole modeling procedure is easy and the efficiency can be guaranteed as we have discussed in the last section. In this paper, the parallel thinning method [28] is used to extract the vascular skeleton. As this method may produce spurious branches during voxel removing, we take the locally estimated diameter of vasculature into account, and represent the vascular skeleton as a

connected graph to improve the limitation. Furthermore, the vascular volume data is manually segmented by the medical trainees, the accuracy of the data can be ensured. So the influence of this limitation is not obvious in our application. Also, multi-branching models with more than four branchings are not supported in our methodology, though they are very rare in human vascular system. In the future work, we will apply our methods to build 3D vascular models for other parts of human beings and aim at employing these built vasculature models in simulation-based VIR training and planning systems.

#### Conflict of interest statement

We declare no conflict of interest.

#### Acknowledgment

This work described in this paper was supported by a grant from the NSFC/RGC Joint Research Scheme sponsored by the Research Grants Council of Hong Kong and the National Natural Science Foundation of China (Project nos. N\_CUHK409/09 and 60931160441), a grant from the National Science Foundation of China (Project No. 61233012) and a grant from Specialized Research Fund for the Doctoral Program of Higher Education (Project No. 20120181130007).

#### References

- [1] W.E. Lorensen, H.E. Cline, Marching cubes: a high resolution 3D surface construction algorithm, *Comput. Graphics* 21 (4) (1987) 163–169.
- [2] T. Poston, T.-T. Wong, P.-A. Heng, Multiresolution isosurface extraction with adaptive skeleton climbing, *Comput. Graphics Forum* 17 (3) (1998) 137–148.
- [3] H.E. Cline, W.E. Lorensen, R. Kikinis, F. Jolesz, Three dimensional segmentation of mr images of the head using probability and connectivity, *J. Comput. Assisted Tomogr.* 14 (6) (1990) 1037–1045.
- [4] Y. Wang, C.K. Chui, Y. Cai, K. Mak, Construction of topological structure of 3D coronary vessels for analysis of catheter navigation in interventional cardiology simulation, in: Y. Kim, S.K. Mun (Eds.), *Medical Imaging 1998: Image Display*, vol. 3335, SPIE, San Diego, CA, USA, 1998, pp. 390–398.
- [5] F. Ritter, C. Hansen, V. Dicken, O. Konrad, B. Preim, H.-O. Peitgen, Real-time illustration of vascular structures, *IEEE Trans. Visualization Comput. Graphics* 12 (5) (2006) 877–884.
- [6] C. Barillot, B. Gibaud, J.-M. Scarabin, J.-L. Coatrieux, 3D reconstruction of cerebral blood vessels, *IEEE Comput. Graphics Appl.* 5 (12) (1985) 13–19.
- [7] Y. Masutani, K. Masamune, T. Dohi, Region-growing-based feature extraction algorithm for tree-like objects, in: *Proceedings of the Visualization in Biomedical Computing*, vol. 1131, Springer, LNCS, 1996, pp. 167–171.
- [8] H. Hahn, B. Preim, D. Selle, H.-O. Peitgen, Visualization and interaction techniques for the exploration of vascular structures, in: *Proceedings of the Visualization 2001 (VIS '01)*, 2001, pp. 395–578.
- [9] K.H. Höhne, B. Pflessner, A. Pommert, M. Riemer, R. Schubert, T. Schiemann, U. Tiege, U. Schumacher, A realistic model of the inner organs from the visible human data, in: *Proceedings of the Third International Conference on Medical Image Computing and Computer-Assisted Intervention*, Springer-Verlag, London, UK, 2000, pp. 776–785.
- [10] P. Felkel, A.L. Fuhrmann, F. Al, A. Kanitsar, R. Wegenkittl, Surface reconstruction of the branching vessels for augmented reality aided surgery, in: J. Jan, J. Kozumplík, I. Provatnik (Eds.), *Biosignal'02*, vol. 16, VUTIUM Press, 2002, pp. 252–254.
- [11] P. Felkel, R. Wegenkittl, K. Buhler, Surface models of tube trees, in: *Proceedings of the 2004 Computer Graphics International*, 2004, pp. 70–77.
- [12] A. Bornik, B. Reitingen, R. Beichel, Reconstruction and representation of tubular structures using simplex meshes, in: *Proceedings of the Winter School of Computer Graphics (WSCG) 2005*, Press, 2005, pp. 61–65.
- [13] J. Bloomenthal, K. Shoemake, Convolution surfaces, computer graphics, in: *Proceedings of the ACM SIGGRAPH*, vol. 25(4), 1991, pp. 251–256.
- [14] J. Bloomenthal, An implicit surface polygonizer, *Graphics Gems IV*, Academic Press Professional, Inc., San Diego, CA, USA, 1994, pp. 324–349.
- [15] S. Oeltze, B. Preim, Visualization of vascular structures with convolution surfaces, in: *Proceedings of IEEE/Eurographics Symposium on Visualization (VisSym)*, 2004, pp. 311–320.
- [16] S. Oeltze, B. Preim, Visualization of vascular structures with convolution surfaces: method validation, and evaluation, *IEEE Trans. Med. Imaging* 25 (4) (2005) 540–549.

- [17] I. Volkau, W. Zheng, R. Baimouratov, A. Aziz, W.L. Nowinski, Geometric modeling of the human normal cerebral arterial system, *IEEE Trans. Med. Imaging* 24 (4) (2005) 529–539.
- [18] X. Ye, Y.-Y. Cai, C. Chui, J.H. Anderson, Constructive modeling of g1 bifurcation, *Comput. Aided Geometric Des.* 19 (2002) 513–531.
- [19] Y.-Y. Cai, X. Ye, C. Chui, J.H. Anderson, Constructive algorithms for gc1 generation of vascular network, in: *Advances in Engineering Software*, vol. 34, Elsevier, Amsterdam, The Netherlands, 2003, pp. 439–450.
- [20] M. Piccinelli, A. Veneziani, D.A. Steinman, A. Remuzzi, L. Antiga, A framework for geometric analysis of vascular structures: application to cerebral aneurysms, *IEEE Trans. Med. Imaging* 28 (8) (2009) 1141–1155.
- [21] R. Chitra, Trifurcation of the right common carotid artery, *Indian J. Plast. Surg.* 41 (2008) 85–88.
- [22] Y. Zhang, Y. Bazilevs, S. Goswami, C.L. Bajaj, T.J. Hughes, Patient-specific vascular nurbs modeling for isogeometric analysis of blood flow, in: *Proceedings of the 15th International Meshing Roundtable*, Springer-Verlag, 2006, pp. 73–92.
- [23] W. Wang, B. Joe, Robust computation of the rotation minimizing frame for sweep surface modeling, *Comput.-Aided Des.* 29 (5) (1997) 379–391.
- [24] G. Elber, Global error bounds and amelioration of sweep surfaces, *Comput.-Aided Des.* 29 (6) (1997) 441–447.
- [25] S. Azernikov, Computer aided design of ventilation tubes for customized hearing aid devices, *Comput. Aided Des.* 42 (2010) 87–94.
- [26] P.J. Frey, H. Borouchaki, Surface mesh evaluation, in: *Proceedings of the 6th International Meshing Roundtable*, ParkCity, UT, USA, 1997, pp. 363–373.
- [27] P.J. Frey, H. Borouchaki, Surface mesh quality evaluation, *Int. J. Numer. Methods Eng.* 45 (1999) 101–118.
- [28] Y.F. Tsao, K.S. Fu, A parallel thinning algorithm for 3D pictures, *Comput. Graphics Image Process.* 17 (4) (1981) 315–331.
- [29] A.J. Hanson, Constrained optimal framings of curves and surfaces using quaternion gauss maps, in: *Proceedings of the Visualization '98*, IEEE Computer Society Press, 1998, pp. 375–382.
- [30] R.L. Bishop, There is more than one way to frame a curve, *Am. Math. Mon.* 82 (3) (1975) 246–251.
- [31] A.J. Hanson, H. Ma, Quaternion frame approach to streamline visualization, *IEEE Trans. Visualization Comput. Graphics* 1 (1995) 164–174.
- [32] J. Hoschek, D. Lasser, *Fundamentals of Computer Aided Geometric Design*, A.K. Peters Ltd., Natick, MA, USA, 1993.
- [33] B. Lloyd, G. Székely, M. Harders, Identification of spring parameters for deformable object simulation, *IEEE Trans. Visualization Comput. Graphics* 13 (2007) 1081–1094.
- [34] P. Meyers, H. Schumacher, R. Higashida, C. Derdeyn, G. Nesbit, D. Sacks, L. Wechsler, J. Bederson, S. Lavine, P. Rasmussen, Reporting standards for endovascular repair of saccular intracranial cerebral aneurysms, *AJNR Am. J. Neuroradiol.* 31 (1) (2010) E12–24.

**Jixiang Guo** is an assistant professor in Sichuan University's College of Computer Science. Her research interests include VR, computer animation, soft-tissue deformation and computer-assisted surgery simulation. Guo received her Ph.D. from the Chinese University of Hong Kong's Department of Computer Science and Engineering.

**Shun Li** is a postdoctoral fellow in computer science and engineering at the Chinese University of Hong Kong. His research interests include VR, surgical simulation and physical modeling. Li received an M.Phil. from the Chinese Academy of Sciences' Graduate University.

**Yim-Pan Chui** is a research staff in the Chinese University of Hong Kong's Department of Computer Science and Engineering. His research interests are scientific visualization and VR. Chui received an M.Phil. in computer science from the Chinese University of Hong Kong.

**Jing Qin** is an associate professor in Center for Human–Computer Interaction, Shenzhen Institutes of Advanced Technology, Chinese Academy of Sciences. His research interests are VR-based surgical simulation, multisensory human–computer interaction and biomechanical modeling. Qin received his Ph.D. from the Chinese University of Hong Kong's Department of Computer Science and Engineering.

**Pheng-Ann Heng** is a professor in the Chinese University of Hong Kong's Department of Computer Science and Engineering. His research interests include VR applications in medicine, visualization, medical imaging, human–computer interaction and computer graphics. Heng received his Ph.D. in computer science from Indiana University.